



Third-order orbital corner state and its realization in acoustic crystals

Jiyu Wang ¹, Ying Chen,² and Xiancong Lu ^{1,*}

¹*Department of Physics, Xiamen University, Xiamen 361005, China*

²*Department of Physics, College of Information Science and Engineering, Huaqiao University, Xiamen 361021, China*

(Dated: November 21, 2024)

Three dimensional (3D) third-order topological insulators (TIs) have zero-dimensional (0D) corner states, which are three dimensions lower than bulk. Here we investigate the third-order TIs on breathing pyrochlore lattices with p -orbital freedom. The tight-binding Hamiltonian is derived for the p -orbital model, in which we find that the two orthogonal π -type (transverse) hoppings are the key to open a band gap and obtain higher-order topological corner states. We introduce the Z_4 berry phase to characterize the bulk topology and analysis the phase diagram. The corner states, demonstrated in a finite structure of a regular tetrahedron, exhibit rich 3D orbital configurations. Furthermore, we design an acoustic system to introduce the necessary π -type hopping and successfully observe the orbital corner states. Our work extends topological orbital corner states to third-order, which enriches the contents of orbital physics and may lead to applications in novel topological acoustic devices.

I. INTRODUCTION

Topological insulators (TIs), well known for their bulk–boundary correspondence, are new states of quantum matter with protected gapless edge or surface states [1–8]. In recent years, the concept of higher-order topological insulators (HOTIs) have been put forward, which host gapless hinge or corner states at lower dimensions instead of edge or surface states [9–14]. The HOTIs are extensively studied in two-dimensional (2D) and three-dimensional (3D) systems [15, 66, 67], and have even yielded applications such as corner state lasers [16, 17, 44].

Breathing pyrochlore lattices, the 3D extension of breathing kagome lattices, have been experimentally realized in A-site ordered spinel oxides [20]. Various phenomena have been revealed, such as the magnetic phase transitions [24], the unusual octupolar paramagnet [25], the origin of geometrical frustration [26] and the spin resonances in the magnetically ordered state [28]. Regarding the theoretical works about quantum magnetism on breathing pyrochlore lattices, Weyl magnons have been proposed [23], magnetic phases in the presence of competing interactions have been studied [65], and a spin liquid described by rank-2 $U(1)$ gauge theory has been demonstrated [27]. Recently, the higher-order topology on breathing pyrochlore lattices also attracts many attentions: the topology is characterized by the quantized polarization [21, 57]; a generic recipe for exactly solvable “boundary” states is proposed [56]; the corner states are successfully observed in the acoustic metamaterials [22]. Despite these exciting discoveries, the study of orbital physics in breathing pyrochlore lattices has been largely overlooked.

Over the past few decades, orbital physics has been extensively studied in transition metal compounds [29, 58] and ultracold atomic systems in optical lattices [30, 61]. When occupying p -bands of optical lattices, the orbital order and Mott-insulating state have been proposed for the spinless fermions [59, 72], and the orbital superfluidity has been demonstrated for bosons [32, 62]. In recent years, topological properties of p -orbital systems have received significant research attention. The topological edge states of p -orbital were observed in photonic crystals [63] and acoustic res-

onator chains [73]. The p -orbital modes were also utilized to generate synthetic magnetic flux in a quadrupole topological photonic lattice [60]. Moreover, the second-order p -orbital corner states have been theoretically proposed in (2D) breathing kagome lattice [18], which are successfully realized using photonic systems [19]. While there are works in literature extending the p -orbital system to three dimensions [37, 55, 68–70], third-order topological states in 3D orbital systems have not been explored before. This will be the main topic of this paper.

We will investigate the third-order TIs in a p -orbital breathing pyrochlore lattice, by taking into account all processes of p -orbital hoppings in 3D space. We will also demonstrate the orbital corner states in an acoustic system. The paper is organized as follows: In Sec. II, we introduce the tight-binding Hamiltonian for p -orbital model, where we emphasize the importance of two orthogonal π -type hopping in 3D lattice. In Sec. III, we study the bulk topological properties of p -orbital breathing pyrochlore lattice, which includes the band structure in special parameters, and the Z_4 berry phase for three bands and six bands under the band gap. We find two quantized values, 0.25 and 0.5, for the Z_4 berry phase (mod 2π) in this model. In Sec. IV, we construct a four-layer regular tetrahedral finite structure to demonstrate the zero-energy corner state as well as their rich orbital configurations. In Sec. V, the p -orbital corner states are realized in acoustic system by using numerical simulation. Finally, we provide a summary in Sec. VI

II. TIGHT-BINDING HAMILTONIAN

The structure of breathing pyrochlore lattices is shown in Fig. 1(a), where A , B , C and D denote four sites in a unit cell. The t_1 and t_2 are intracell and intercell hopping amplitudes respectively where breathing hopping ($t_1 \neq t_2$) leads to the HOTIs [21]. We then construct the tight-binding Hamiltonian of breathing pyrochlore lattice with p orbitals. For a 3D system, each lattice site allows for three p orbitals: the p_x , p_y and p_z orbitals. There are basically two types of hoppings, *i.e.*, the σ -type (longitudinal) and π -type (transverse), whose amplitudes are represented by t_σ and t_π re-

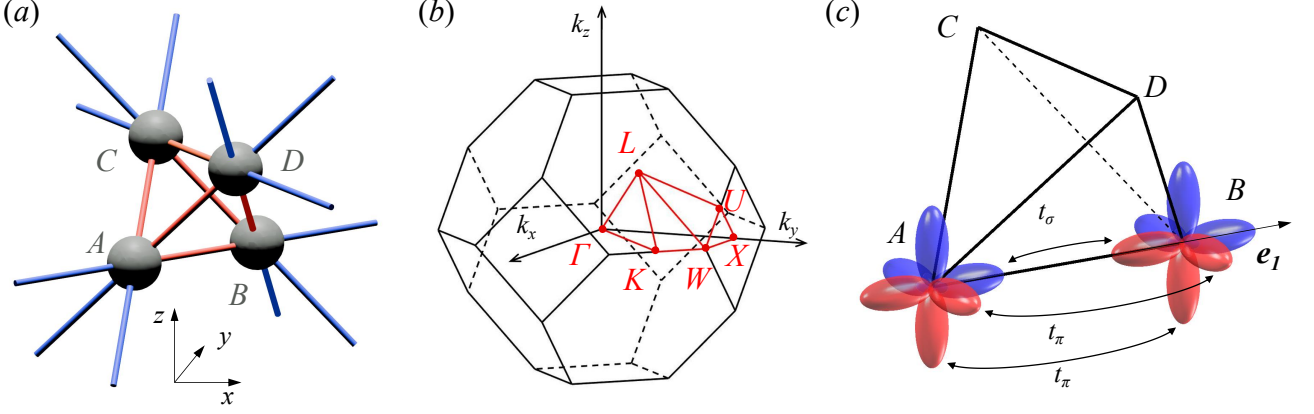


FIG. 1. (a) The structure of breathing pyrochlore lattices in real space. Gray solid spheres represent four sites in a unit cell, which make up a regular tetrahedron. The red and blue cylinders indicate the hoppings inside and between unit cells. (b) The first Brillouin zone with high symmetry points (Γ , X , W , U , L , K) in k space. (c) The σ and π types of hoppings for p orbitals. For 3D lattices, two orthogonal π hoppings should be taken into account. The red and blue ellipsoids represent the signs (+ and -) of two lobes of a p orbital.

spectively [18, 35, 36, 51, 52]. Note that only one π -type hopping needs to be considered for the 2D p -orbital models studied in previous works [18, 35, 36, 51, 52]. However, for 3D models, one needs to take into account two orthogonal π -type hoppings, to fully capture the π -type hopping process; see Fig. 1(c).

For the σ -type (longitudinal) hopping, we define six vectors along the hopping directions between two nearest-neighbor lattice sites,

$$\begin{aligned} \mathbf{e}_1 &= (1, 1, 0), & \mathbf{e}_2 &= (0, 1, 1), & \mathbf{e}_3 &= (1, 0, 1), \\ \mathbf{e}_4 &= (-1, 0, 1), & \mathbf{e}_5 &= (0, -1, 1), & \mathbf{e}_6 &= (1, -1, 0). \end{aligned} \quad (1)$$

The p orbitals can be projected along these hopping directions of lattices. The six projection operators p_i^σ ($i = 1, 2, \dots, 6$) can be written as

$$\begin{aligned} p_{1,6}^\sigma &= \mathbf{e}_{1,6} \cdot \mathbf{p} = p_x \pm p_y, \\ p_{2,5}^\sigma &= \mathbf{e}_{2,5} \cdot \mathbf{p} = \pm p_y + p_z, \\ p_{3,4}^\sigma &= \mathbf{e}_{3,4} \cdot \mathbf{p} = \pm p_x + p_z, \end{aligned} \quad (2)$$

in which the p -orbital operator \mathbf{p} is defined on the p_x , p_y and p_z basis: $\mathbf{p} = (p_x, p_y, p_z)^T$.

For the π -type (transverse) hopping, we define two sets of vectors \mathbf{m}_i and \mathbf{n}_i ($i = 1, 2, \dots, 6$) which are perpendicular to the hopping directions:

$$\begin{aligned} \mathbf{m}_1 &= (1, -1, 0), & \mathbf{m}_2 &= (0, 1, -1), & \mathbf{m}_3 &= (1, 0, -1), \\ \mathbf{m}_4 &= (1, 0, 1), & \mathbf{m}_5 &= (0, 1, 1), & \mathbf{m}_6 &= (1, 1, 0). \end{aligned} \quad (3)$$

$$\begin{aligned} \mathbf{n}_1 &= (0, 0, \sqrt{2}), & \mathbf{n}_2 &= (\sqrt{2}, 0, 0), & \mathbf{n}_3 &= (0, \sqrt{2}, 0), \\ \mathbf{n}_4 &= (0, -\sqrt{2}, 0), & \mathbf{n}_5 &= (-\sqrt{2}, 0, 0), & \mathbf{n}_6 &= (0, 0, -\sqrt{2}). \end{aligned} \quad (4)$$

It is worth noting that the vectors \mathbf{e}_i , \mathbf{m}_i and \mathbf{n}_i are pairwise orthogonal to each other. Then, two sets of orthogonal projection operators ($p_i^{\pi 1}$ and $p_i^{\pi 2}$) perpendicular to the hopping direction are given by

$$\begin{aligned} p_{1,6}^{\pi 1} &= \mathbf{m}_{1,6} \cdot \mathbf{p} = p_x \mp p_y, & p_{2,5}^{\pi 1} &= \mathbf{m}_{2,5} \cdot \mathbf{p} = p_y \mp p_z, \\ p_{3,4}^{\pi 1} &= \mathbf{m}_{3,4} \cdot \mathbf{p} = p_x \mp p_z, & p_{1,6}^{\pi 2} &= \mathbf{n}_{1,6} \cdot \mathbf{p} = \pm \sqrt{2} p_z, \\ p_{2,5}^{\pi 2} &= \mathbf{n}_{2,5} \cdot \mathbf{p} = \pm \sqrt{2} p_x, & p_{3,4}^{\pi 2} &= \mathbf{n}_{3,4} \cdot \mathbf{p} = \pm \sqrt{2} p_y. \end{aligned} \quad (5)$$

With these definitions, we obtain the real-space Hamiltonian for the p -orbital breathing pyrochlore lattices,

$$\begin{aligned} H &= - \sum_{\mathbf{r}} \left[t_{1\sigma} (a_{\mathbf{r},1}^{\sigma\dagger} b_{\mathbf{r},1}^\sigma + a_{\mathbf{r},2}^{\sigma\dagger} c_{\mathbf{r},2}^\sigma + a_{\mathbf{r},3}^{\sigma\dagger} d_{\mathbf{r},3}^\sigma \right. \\ &\quad + b_{\mathbf{r},4}^{\sigma\dagger} c_{\mathbf{r},4}^\sigma + b_{\mathbf{r},5}^{\sigma\dagger} d_{\mathbf{r},5}^\sigma + c_{\mathbf{r},6}^{\sigma\dagger} d_{\mathbf{r},6}^\sigma) \\ &\quad + t_{2\sigma} (a_{\mathbf{r}+\mathbf{e}_1,1}^{\sigma\dagger} b_{\mathbf{r},1}^\sigma + a_{\mathbf{r}+\mathbf{e}_2,2}^{\sigma\dagger} c_{\mathbf{r},2}^\sigma + a_{\mathbf{r}+\mathbf{e}_3,3}^{\sigma\dagger} d_{\mathbf{r},3}^\sigma \\ &\quad + b_{\mathbf{r}+\mathbf{e}_4,4}^{\sigma\dagger} c_{\mathbf{r},4}^\sigma + b_{\mathbf{r}+\mathbf{e}_5,5}^{\sigma\dagger} d_{\mathbf{r},5}^\sigma + c_{\mathbf{r}+\mathbf{e}_6,6}^{\sigma\dagger} d_{\mathbf{r},6}^\sigma) \\ &\quad + t_{1\pi} (a_{\mathbf{r},1}^{\pi\dagger} b_{\mathbf{r},1}^\pi + a_{\mathbf{r},2}^{\pi\dagger} c_{\mathbf{r},2}^\pi + a_{\mathbf{r},3}^{\pi\dagger} d_{\mathbf{r},3}^\pi \\ &\quad + b_{\mathbf{r},4}^{\pi\dagger} c_{\mathbf{r},4}^\pi + b_{\mathbf{r},5}^{\pi\dagger} d_{\mathbf{r},5}^\pi + c_{\mathbf{r},6}^{\pi\dagger} d_{\mathbf{r},6}^\pi) \\ &\quad + t_{2\pi} (a_{\mathbf{r}+\mathbf{e}_1,1}^{\pi\dagger} b_{\mathbf{r},1}^\pi + a_{\mathbf{r}+\mathbf{e}_2,2}^{\pi\dagger} c_{\mathbf{r},2}^\pi + a_{\mathbf{r}+\mathbf{e}_3,3}^{\pi\dagger} d_{\mathbf{r},3}^\pi \\ &\quad + b_{\mathbf{r}+\mathbf{e}_4,4}^{\pi\dagger} c_{\mathbf{r},4}^\pi + b_{\mathbf{r}+\mathbf{e}_5,5}^{\pi\dagger} d_{\mathbf{r},5}^\pi + c_{\mathbf{r}+\mathbf{e}_6,6}^{\pi\dagger} d_{\mathbf{r},6}^\pi) \left. \right] \\ &\quad + H.c. \end{aligned} \quad (6)$$

in which each π -type hopping term (see the last 12 terms

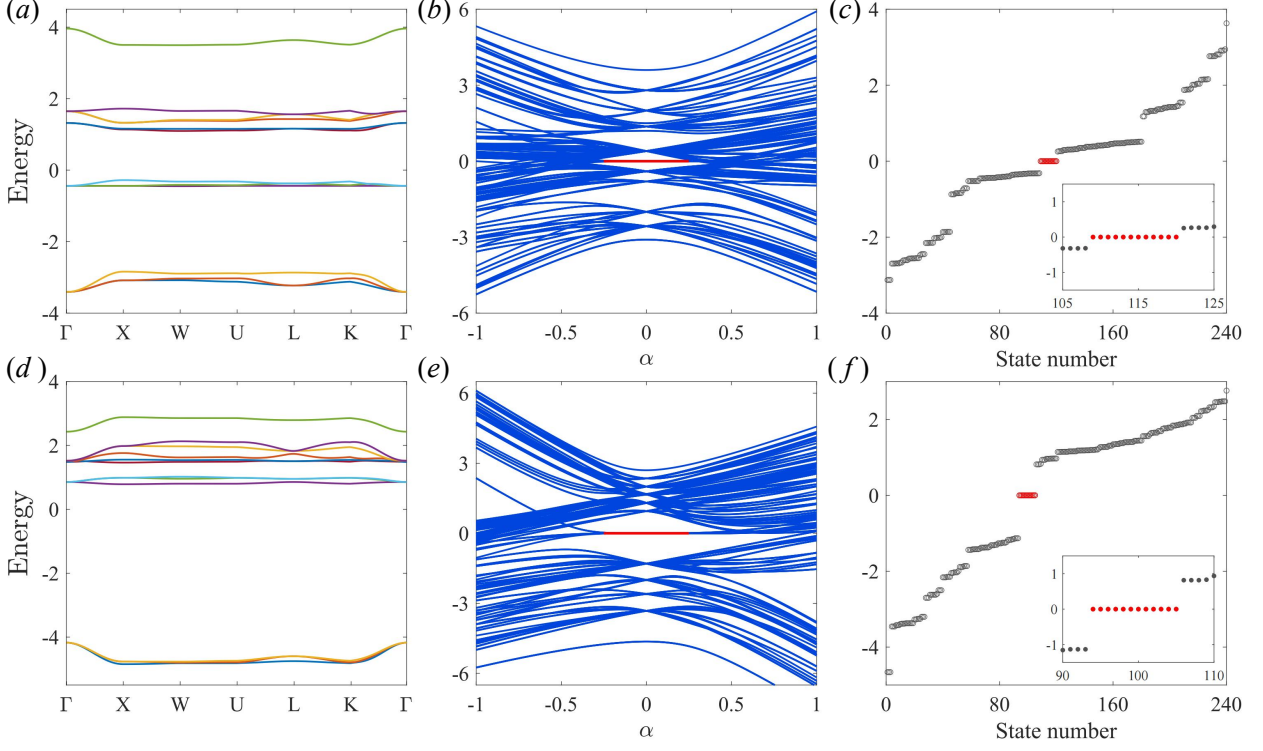


FIG. 2. (a), (d) Band structures of p -orbital breathing pyrochlore lattice in k -space. The values of hopping amplitude are (a) $\alpha = 0.1, \beta = 0.2$; six bands under the zero-energy gap; (d) $\alpha = -0.1, \beta = 0.65$; three bands under the zero-energy gap; (b), (c), (e), (f) The energy spectrum of a four-layer ($L=4$) tetrahedron-shaped finite structure of p -orbital breathing pyrochlore lattice. The energy dispersion as a function of α when (b) $\beta = 0.2$ and (e) $\beta = 0.65$. The horizontal red lines indicate the orbital corner states with $E = 0$. The energy as a function of state number when (c) $\alpha = 0.1$ and $\beta = 0.2$, (f) $\alpha = -0.1$ and $\beta = 0.65$. The 12 degenerate corner states are magnified in the inset figures in (c) and (f).

in Eq. (6) includes two identical types of hopping (π_1 and π_2), for example, $a_{\mathbf{r},1}^{\pi_1\dagger} b_{\mathbf{r},1}^{\pi_1} = a_{\mathbf{r},1}^{\pi_1\dagger} b_{\mathbf{r},1}^{\pi_1} + a_{\mathbf{r},1}^{\pi_2\dagger} b_{\mathbf{r},1}^{\pi_2}$. $t_{1\sigma}$ and $t_{1\pi}$ ($t_{2\sigma}$ and $t_{2\pi}$) represent the amplitudes of the σ and π types of hopping inside (between) unit cells. $a_{\mathbf{r}}^{\sigma}$ ($a_{\mathbf{r}}^{\pi}$), $b_{\mathbf{r}}^{\sigma}$ ($b_{\mathbf{r}}^{\pi}$), $c_{\mathbf{r}}^{\sigma}$ ($c_{\mathbf{r}}^{\pi}$), and $d_{\mathbf{r}}^{\sigma}$ ($d_{\mathbf{r}}^{\pi}$) are the σ (π) type of annihilating projection operators at the sites A, B, C , and D , respectively, in the unit cell located at position \mathbf{r} . The right-side subscript i in operator $a_{\mathbf{r},i}^{\sigma}$ ($a_{\mathbf{r},i}^{\pi}$) indicates that the projection is along the direction e_i .

After making Fourier transformation to Eq. (6) and introducing a 12-component spinor $\psi = [a_{\mathbf{k},x}, a_{\mathbf{k},y}, a_{\mathbf{k},z}, b_{\mathbf{k},x}, b_{\mathbf{k},y}, b_{\mathbf{k},z}, c_{\mathbf{k},x}, c_{\mathbf{k},y}, c_{\mathbf{k},z}, d_{\mathbf{k},x}, d_{\mathbf{k},y}, d_{\mathbf{k},z}]^T$, the Hamiltonian can be rewritten as $H = \sum_{\mathbf{k}} \psi^\dagger H(\mathbf{k}) \psi$. The matrix $H(\mathbf{k})$ is derived as follows,

$$H(\mathbf{k}) = - \begin{pmatrix} 0 & D_1 & D_2 & D_3 \\ D_1^\dagger & 0 & D_4 & D_5 \\ D_2^\dagger & D_4^\dagger & 0 & D_6 \\ D_3^\dagger & D_5^\dagger & D_6^\dagger & 0 \end{pmatrix}_{12 \times 12}, \quad (7)$$

in which the matrices are given by

$$D_1 = \begin{pmatrix} 1 & 1 & 0 \\ 1 & 1 & 0 \\ 0 & 0 & 0 \end{pmatrix} f_{1\sigma} + \begin{pmatrix} 1 & -1 & 0 \\ -1 & 1 & 0 \\ 0 & 0 & 2 \end{pmatrix} f_{1\pi} \quad (8)$$

$$D_2 = \begin{pmatrix} 0 & 0 & 0 \\ 0 & 1 & 1 \\ 0 & 1 & 1 \end{pmatrix} f_{2\sigma} + \begin{pmatrix} 2 & 0 & 0 \\ 0 & 1 & -1 \\ 0 & -1 & 1 \end{pmatrix} f_{2\pi} \quad (9)$$

$$D_3 = \begin{pmatrix} 1 & 0 & 1 \\ 0 & 0 & 0 \\ 1 & 0 & 1 \end{pmatrix} f_{3\sigma} + \begin{pmatrix} 1 & 0 & -1 \\ 0 & 2 & 0 \\ -1 & 0 & 1 \end{pmatrix} f_{3\pi} \quad (10)$$

$$D_4 = \begin{pmatrix} 1 & 0 & -1 \\ 0 & 0 & 0 \\ -1 & 0 & 1 \end{pmatrix} f_{4\sigma} + \begin{pmatrix} 1 & 0 & 1 \\ 0 & 2 & 0 \\ 1 & 0 & 1 \end{pmatrix} f_{4\pi} \quad (11)$$

$$D_5 = \begin{pmatrix} 0 & 0 & 0 \\ 0 & 1 & -1 \\ 0 & -1 & 1 \end{pmatrix} f_{5\sigma} + \begin{pmatrix} 2 & 0 & 0 \\ 0 & 1 & 1 \\ 0 & 1 & 1 \end{pmatrix} f_{5\pi} \quad (12)$$

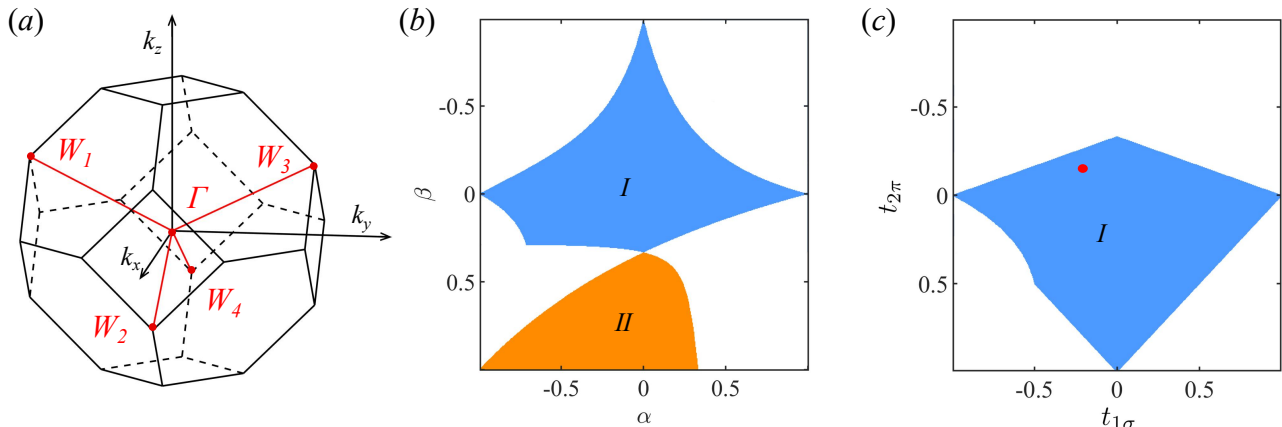


FIG. 3. Bulk topological properties of p -orbital breathing pyrochlore lattice. (a) Four integral paths (marked by red lines) in Brillouin zone: $P_1 : W_1 \rightarrow \Gamma \rightarrow W_2$, $P_2 : W_2 \rightarrow \Gamma \rightarrow W_3$, $P_3 : W_3 \rightarrow \Gamma \rightarrow W_4$, $P_4 : W_4 \rightarrow \Gamma \rightarrow W_1$. (b) and (c) Bulk topological phase diagram of Z_4 berry phase (mod 2π). The orange area II corresponds to a value of 0.25 for the lowest three bands ($\nu=3$); The blue area I corresponds to a value of 0.5 for the lowest six bands ($\nu=6$); The position of the red round dot in (c) corresponds to the parameters of the acoustic model.

$$D_6 = \begin{pmatrix} 1 & -1 & 0 \\ -1 & 1 & 0 \\ 0 & 0 & 0 \end{pmatrix} f_{6\sigma} + \begin{pmatrix} 1 & 1 & 0 \\ 1 & 1 & 0 \\ 0 & 0 & 2 \end{pmatrix} f_{6\pi} \quad (13)$$

with $f_{i\sigma} = t_{1\sigma} + t_{2\sigma} e^{-i\mathbf{k}\cdot\mathbf{e}_i}$ and $f_{i\pi} = t_{1\pi} + t_{2\pi} e^{-i\mathbf{k}\cdot\mathbf{e}_i}$.

III. BULK TOPOLOGICAL PROPERTIES

The Hamiltonian in Eq. (6) contains four hopping parameters: $t_{1\pi}$, $t_{1\sigma}$, $t_{2\pi}$, and $t_{2\sigma}$. In systems such as photonic lattices, where the intercell and intracell hoppings are tuned by adjusting the distance between two photonic cavities [18], the ratio between π -type and σ -type hoppings remains approximately constant, i.e., $t_{1\pi}/t_{1\sigma} \approx t_{2\pi}/t_{2\sigma}$. We therefore introduce two additional parameters: $\alpha = t_{1\pi}/t_{2\pi} = t_{1\sigma}/t_{2\sigma}$ and $\beta = t_{1\pi}/t_{1\sigma} = t_{2\pi}/t_{2\sigma}$, and set $t_{2\sigma}$ as energy unit ($t_{2\sigma} = 1$). This way allows us to conveniently discuss the topological phase diagram in the $\alpha - \beta$ plane. For the acoustic systems to be discussed in Sec. V, the ratio between π -type and σ -type hoppings is no longer constant ($t_{1\pi}/t_{1\sigma} \neq t_{2\pi}/t_{2\sigma}$, see Fig. 6(e)). Hence, one must consider the topologies in the four-parameter space. In such case, we will explicitly provide the values of all four hopping parameters.

The Brillouin zone of breathing pyrochlore lattice with high symmetry points is shown in Fig. 1(b), which forms a truncated octahedron. The energy bands are obtained by diagonalizing the k -space Hamiltonian in Eq. (7). There are four sites in a unit cell with three p orbitals in each site, leading to 12 bands in this model. Here, we show the band structures in Fig. 2 where the zero energy appears in the band gap. The number of bands below the zero energy gap varies as the values of the parameters α and β change. Typically,

Fig. 2(a) exhibits six bands under the zero energy gap with a relatively small value of β , while Fig. 2(d) exhibits three bands under the gap with a relatively large value of β . It is worth mentioning that the bands are degenerate when $\beta = 1$, that is, all orbitals are isotropic. In this case, the band structure of our model go back to s -band model with three bands [21], where the flat band is six-fold degenerate and the other two are three-fold degenerate.

Z_Q berry phase is one of the symmetry protected topological invariants for HOTIs [38–40]. Inspired by the Z_3 berry phase for the breathing kagome lattice [18, 41], the Z_4 berry phase for the breathing square lattice [42] and recently Z_6 berry phase for distortionary honeycomb lattice [74], we calculate the Z_4 berry phase in momentum space for the breathing pyrochlore lattice. The elements of the Berry connection matrix ($\nu \times \nu$) are

$$\mathbf{A}_{mn}(\mathbf{k}) = i\langle u_m(\mathbf{k}) | \partial_{\mathbf{k}} | u_n(\mathbf{k}) \rangle, \quad m, n = 1, 2, \dots, \nu, \quad (14)$$

where $|u_n(\mathbf{k})\rangle$ is the periodic Bloch wave function for the n th bands, and ν is the number of bands under a band gap. For the lowest ν bands under a gap, the Berry phase is defined as

$$\theta^\nu = \int_{P_i} \text{Tr}[\mathbf{A}(\mathbf{k})] d\mathbf{k}, \quad (15)$$

in which P_i ($i = 1, 2, 3, 4$) represents an integral path ($W_i \rightarrow \Gamma \rightarrow W_{i+1}$ with $W_5 = W_1$) in the Brillouin zone when using the Wilson-loop approach [49, 50], as shown in Fig. 3(a). In fact, the Z_4 Berry phase in momentum space here is equivalent to the local gauge twists berry phase in parameter space discussed in Refs. [39, 43]. Besides, the four high-symmetry points W_1 , W_2 , W_3 , and W_4 , shown in Fig. 3(a), are equivalent because of the S_4 symmetry. Therefore, there are four

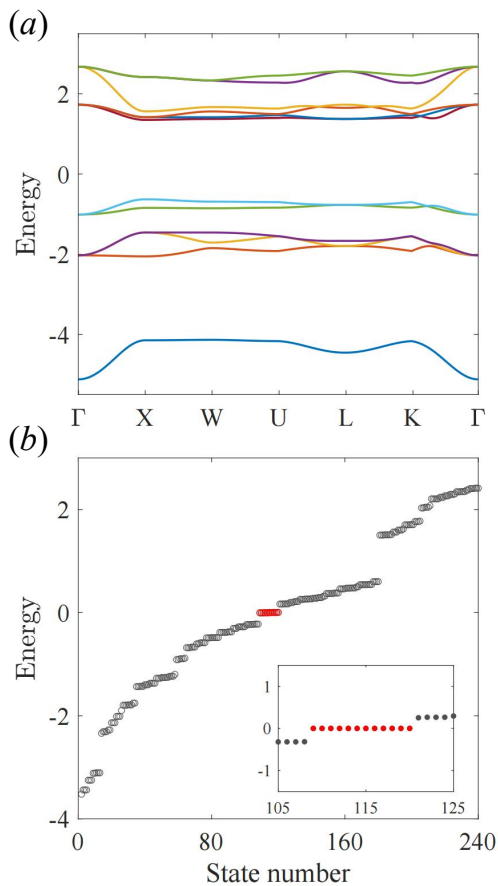


FIG. 4. (a) Band structures of p -orbital breathing pyrochlore lattice. (b) The energy spectrum of a four-layer ($L = 4$) tetrahedron-shaped finite structure. In both subfigures, the hopping amplitudes are set to $t_{1\sigma} = -0.19, t_{2\sigma} = -1, t_{1\pi} = 0, t_{2\pi} = 0.18$. The 12 degenerate corner states are magnified in the inset of subfigure (b).

equivalent integral paths ($P_1 : W_1 \rightarrow \Gamma \rightarrow W_2, P_2 : W_2 \rightarrow \Gamma \rightarrow W_3, P_3 : W_3 \rightarrow \Gamma \rightarrow W_4, P_4 : W_4 \rightarrow \Gamma \rightarrow W_1$) leading to identical θ^ν , that is,

$$\theta^\nu(P_1) = \theta^\nu(P_2) = \theta^\nu(P_3) = \theta^\nu(P_4). \quad (16)$$

Obviously, the sum of the integrals along the four paths ($P_1, P_2, P_3,$ and P_4) is zero:

$$\sum_{i=1}^4 \theta^\nu(P_i) = 0. \quad (17)$$

Therefore, the Z_4 Berry phase is quantized as

$$\theta^\nu \equiv \theta^\nu(P_i) = 2\pi n/4, \quad (n = 0, 1, 2, 3). \quad (18)$$

We demonstrate the bulk topological phase diagram in Fig. 3(b) where the Z_4 berry phase for the lowest three ($\nu = 3, \theta^3/2\pi = 0.25$) and six ($\nu = 6, \theta^6/2\pi = 0.5$) bands are shown. It should be noted that the origin of topology is the adiabatic connection between the energy spectrum at $t_1 \neq 0$ and $t_1 = 0$ [21]. The Z_4 berry phase changes when the band gap is closed and reopened. Since the higher-order

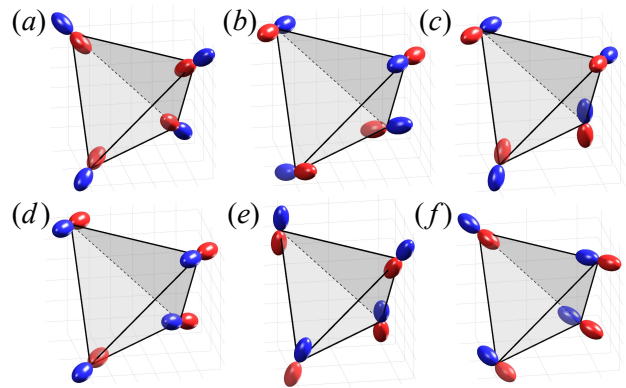


FIG. 5. The orbital configurations of corner states for a four-layer ($L = 4$) tetrahedron-shaped finite structure. (a)-(f) Only the orbitals on the corner are shown. The dashed line represents an edge on the far side of a tetrahedron. The direction of the major axis of the ellipse indicates the direction of the p orbital. The parameters are chosen as $t_{1\sigma} = -0.19, t_{2\sigma} = -1, t_{1\pi} = 0, t_{2\pi} = 0.18$, which are the same as those in Fig. 4.

topological corner states appear at zero energy, we take into account an additional condition when plotting the topological phase diagram: the zero energy states must exist inside a band gap (*i.e.*, the bulk bands cannot cross the zero-energy level). The topologically nontrivial regions in the phase diagram of Fig. 3(b) are actually smaller than those obtained by only considering the Z_4 berry phase. At the same time, the above condition ensures that the nontrivial orange and blue regions in the phase diagram, calculated using different number of bands ($\nu = 3$ and $\nu = 6$), do not overlap and intersect at a point ($\alpha = 0, \beta \approx 0.33$), as shown in Fig. 3(b).

To facilitate a comparison with the simulation results for acoustic crystals presented in Sec. V, we depict in Fig. 4(a) the band structures for a specific set of parameter values: $t_{1\sigma} = -0.19, t_{2\sigma} = -1, t_{1\pi} = 0, t_{2\pi} = 0.18$. Note that $t_{1\pi}/t_{1\sigma} \neq t_{2\pi}/t_{2\sigma}$ in this case. Considering the simulation situation of the acoustic model, we fix two parameters $t_{2\sigma} = -1, t_{1\pi} = 0$, obtaining another phase diagram in Fig. 3(c). The parameter positions corresponding to the acoustic model are represented by the red round dot in blue region.

IV. THE ORBITAL CORNER STATES

Here we investigate the p -orbital corner states in a finite tetrahedral structure for the breathing pyrochlore lattice. We use L , the number of unit cells (the small tetrahedron surrounded by red lines shown in Fig. 1(a)) along one edge of the finite lattice, to define the size of our structure [21]. The total number of unit cells in the finite structure is $L(L+1)(L+2)/6$, corresponding to $4L(L+1)(L+2)/6$ sites and $12L(L+1)(L+2)/6$ p -orbital states. We take $L = 4$ in this work, indicating 20 unit cells, 80 sites, and 240 p -orbital states.

The energy dispersion of a tetrahedron-shaped finite structure, shown in Fig. 2(b) and (e), is obtained by diagonalizing the real-space Hamiltonian in Eq. (6). We choose two

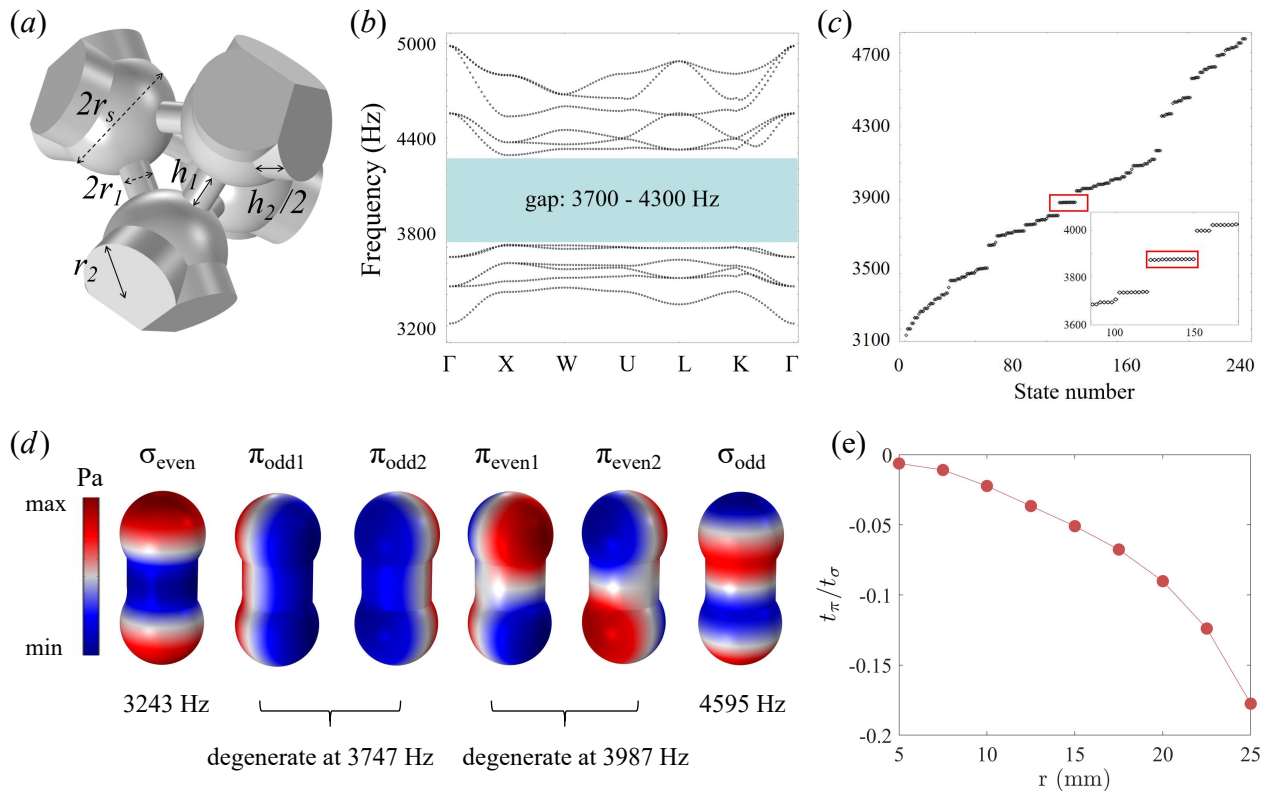


FIG. 6. (a) Schematic diagram for the unit cell of acoustic breathing pyrochlore lattices where $r_s = 30$ mm, $r_1 = 7.6$ mm, $h_1 = 15.8$ mm, $r_2 = 25$ mm and $h_2 = 31.8$ mm. (b) The simulated band structure. (c) Evolution of the spectrum (frequency) of four-layer ($L = 4$) finite structure as a function of state numbers. (d) p -orbital pressure fields of two coupled acoustic resonators. The parameters are set to r_s , r_2 and h_2 in (a). (e) The ratio of t_π and t_σ hopping amplitude as a function of the radius of the cylindrical connector where r_s and h_2 are fixed.

typical sets of parameters to demonstrate the corner states. For the parameters $\alpha = 0.1$, $\beta = 0.2$, the Z_4 berry phase (mod 2π) has a value of 0.5 (see Fig. 3(b)), with six bands under the zero-energy gap in the bulk spectrum (see Fig. 2(a)). Whereas for $\alpha = -0.1$, $\beta = 0.65$, the Z_4 berry phase (mod 2π) has a value of 0.25, with three bands under the zero-energy gap (see Fig. 2(d)). We plot the energy as a function of the number of eigenstates in Fig. 2(c) and (f). Both of them exhibit 12 degenerate zero-energy corner states, as displayed in the enlarged insets. For these two Z_4 berry phases, the orbital configurations of corner states exhibit similar characteristics, since the energy spectra of both phases can be adiabatically connected to the same limit of $t_1 = 0$. It should be pointed out that in realistic system t_π is much smaller than t_σ due to the anisotropy of p orbital. Interestingly, the acoustic system is also a versatile platform to tune the values of t_π and t_σ , similar to the photonic system [18]. We will demonstrate this in the subsequent simulation part in Sec. V.

The range of parameters with distinguishable corner states may be smaller than that predicted by the bulk topological invariants [see Fig. 3(b)]. This is because the localized states of the finite tetrahedral structure (existing on the edges, surfaces etc.) could have energies very close to zero, and therefore obscure the zero-energy corner states. Clearly, the zero-energy states at the right end of the red line in Fig.

2(b) and (e) cannot be distinguished whether they are corner states or not. In addition, the appearance of corner states are strongly affected in two parameter regions around $\beta = 0$ ($t_\pi = 0$) and $\beta = 0.33$, due to the possible mixing with bulk bands. As shown in Fig. 2(b) and (e), the zero-energy band (red line) is located in a gap surrounded by bulk bands. When the value of β is around zero, this gap will disappear, leading to the indistinguishable zero-energy states for corner. When β is around 0.33, some bulk bands will rise up to the zero-energy position, and cover the corner states. This phenomenon ($\beta \approx 0.33$) can also be explained by the band structure obtained from the k -space Hamiltonian, that is, the fourth, fifth, and sixth bands (counting from the bottom) will gradually rise as β increases from -1 to 1. These three bands just pass through the zero-energy level when β is about 0.33.

To compare with the simulation results for the acoustic model, we focus on the following set of parameter values: $t_{1\sigma} = -0.19$, $t_{2\sigma} = -1$, $t_{1\pi} = 0$, $t_{2\pi} = 0.18$. In Fig. 4(b), we plot the energy spectrum of a four-layer ($L = 4$) tetrahedron-shaped finite structure. There are 12 degenerate corner states within a sizable band gap. The orbital configurations of various corner states are displayed in Fig. 5 for this finite structure. For clarity, we only exhibit the p -orbital orientations at four corners. One of the most symmetrical states appears in Fig. 5(a). There are also three orbital configurations in which the orbitals at four corner sites are nearly

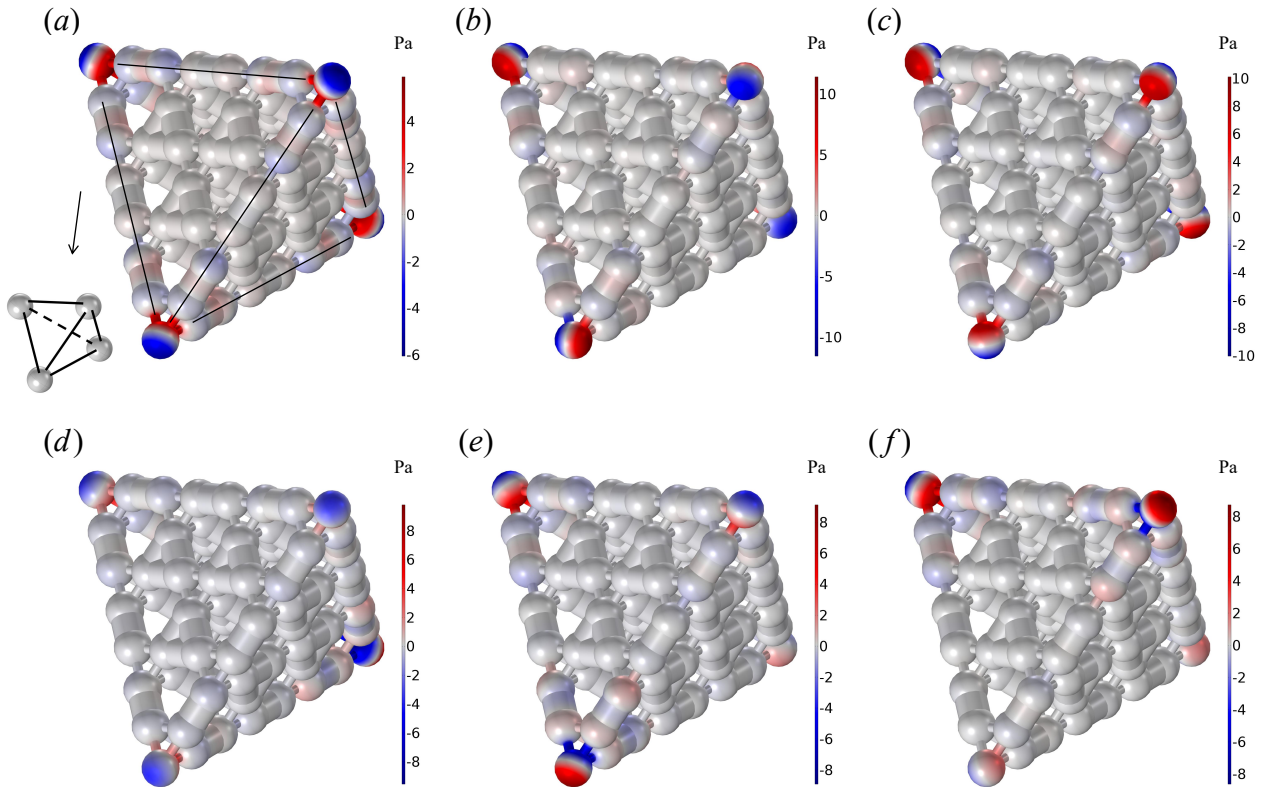


FIG. 7. (a)-(f) The p -orbital acoustic pressure fields of the tetrahedron made of breathing pyrochlore lattices with $L = 4$. In order to illustrate the 3D structure, we add a schematic tetrahedron in the lower-left corner of sub-figure (a) to guide the eye.

parallel, as shown in Fig. 5(d)-(f). The configurations presented in Fig. 5(b) and (c) does not exhibit regular pattern like the above-mentioned cases. Interestingly, the distributions of these configurations can be observed in an acoustic system; see the next section.

V. THE REALIZATION OF ORBITAL CORNER STATES IN ACOUSTIC CRYSTALS

Recently, topological acoustics have been a large research area to mimic topological phenomena in condensed matter system [45–48, 53]. Compared to other systems, topological acoustic crystals have excellent tunability which can be more easily designed into various geometric shapes to achieve corresponding topological properties. At the same time, acoustic properties can be accurately measured in a wide range of laboratory conditions, allowing for direct and convenient acquisition of topological information. Therefore, we use acoustic system to realize our tight-binding model. Instead of using a conventional cylindrical resonators [22, 54], spherical resonators [37, 71] are used to achieve a uniform space for p -orbital couplings.

We perform simulation with finite-element method to calculate the eigenstates of such acoustic breathing pyrochlore lattices, where sound hard boundary condition of all air-solid

interfaces is considered. The density of the air and the speed of sound are set to be 1.25 kg/m^3 and 343 m/s . Unit cell of pyrochlore lattice is shown in Fig. 6(a), the radius r_s of sphere is fixed at 30 mm , the length and radius of the connecting cylinders are used to adjust the strength of different hoppings where one type (t_1) is set with radius r_1 of 7.6 mm and length h_1 of 15.8 mm , the other type (t_2) is 25 mm for the radius r_2 and 31.8 mm for the length h_2 . In simulation, we slightly reduce the radius (to 29.4 mm) of the spherical resonator at four corners, since the effective capacity of the resonator at corner is a bit larger than that in bulk if we use the same radius for all spheres.

In order to introduce π hoppings in this acoustic model, here we consider two coupled spherical resonators connecting by a cylindrical tube whose parameters are set to r_s , r_2 and h_2 . The p -orbital eigenfields are shown in Fig. 6(d) where we can see σ -like and π -like bonding with even or odd parity in such coupled resonators. The hopping amplitudes t_σ and t_π in the acoustic model can be determined by half of the difference between the frequencies of the even and odd hybrid modes of two coupled resonators, i.e., $t_\sigma \propto 1/2(f_{\sigma_{odd}} - f_{\sigma_{even}})$, $t_\pi \propto 1/2(f_{\pi_{odd}} - f_{\pi_{even}})$ [37]. In Fig. 6(e), the ratio of estimated t_π and t_σ is plotted as a function of the radius of the connecting cylinder. As illustrated, a larger cylinder radius introduces a considerable π hopping

amplitude, which can open a gap to harbor the corner states.

The p -orbital band structure, shown in Fig. 6(b), shows a band gap existed in the frequency range from 3700 Hz to 4300 Hz. Besides, the energy spectrum for a 4-layer finite structure is calculated in Fig. 6(c) where 12 degenerate corner states appear in the p -orbital band gap. The acoustic band structure and energy spectrum of the finite structure only qualitatively agree with those of the tight-binding model presented in Fig. 4(a) and (b), where the parameters are estimated from the double-resonator model. The deviation from the tight-binding model can be attributed to the fact that the coupling strength in a three-dimensional acoustic lattice differs from that in the double-resonator model due to the specific interconnections. The acoustic fields of corner states are further displayed in Fig. 7(a-f). We can see that the fields are highly localized on the four corners with different orbital configurations. In detail, Fig. 7(a) displays the most symmetric geometry of p -orbitals pointing towards the center of the tetrahedron, which is consistent with the tight-binding results in Fig. 5(a). Parallel states (see Fig. 7(d-f)) exhibit a tendency for the orbital orientation of all four corners to align in one direction. The results of p -orbital acoustic field patterns are in qualitative agreement with tight-binding model shown in Fig. 5.

VI. CONCLUSION

In summary, we have investigated the third-order topological orbital corner states in the p -orbital breathing pyrochlore lattice. The presence of two orthogonal π -type hopping terms is the crucial factor to obtain the orbital corner states. Without them, the corner states are indistinguishable from the bulk states. Based on the Z_4 berry phase, we investigate the bulk topological properties and obtain the phase diagram, in which two quantized values of Z_4 berry phase (mod 2π), 0.25 and 0.5, correspond to three and six bands below the band gap, respectively. By constructing a four-layer regular tetrahedral finite structure, we demonstrate the existence of corner states and reveal their rich orbital configurations. Finally, we realize the orbital corner states in acoustic crystals and validate the experimental feasibility of the p -orbital model. Our work may further promote the research of high-order topology with orbital freedom.

ACKNOWLEDGMENT

We are grateful for the discussions with Chuanshu Xu, Peng Long and Qiang Wei. We also thank Huanyang Chen for the insightful suggestions. This work is supported by the National Natural Science Foundation of China (Grants No. 11974293) and the Promotion Program for Young and Middle-aged Teacher in Science and Technology Research of Huaqiao University (ZQN-1110).

* Corresponding author: xlu@xmu.edu.cn

- [1] C. L. Kane and E. J. Mele, Z_2 topological order and the quantum spin Hall effect, *Physical review letters* **95**, 146802 (2005).
- [2] C. L. Kane and E. J. Mele, Quantum spin Hall effect in graphene, *Physical review letters* **95**, 226801 (2005).
- [3] B. A. Bernevig, T. L. Hughes, and S.-C. Zhang, Quantum spin Hall effect and topological phase transition in HgTe quantum wells, *Science* **314**, 1757 (2006).
- [4] M. Konig, S. Wiedmann, C. Brune, A. Roth, H. Buhmann, L. W. Molenkamp, X.-L. Qi, and S.-C. Zhang, Quantum spin Hall insulator state in HgTe quantum wells, *Science* **318**, 766 (2007).
- [5] L. Fu, C. L. Kane, and E. J. Mele, Topological insulators in three dimensions, *Physical review letters* **98**, 106803 (2007).
- [6] J. E. Moore, The birth of topological insulators, *Nature* **464**, 194 (2010).
- [7] M. Z. Hasan and C. L. Kane, Colloquium: topological insulators, *Reviews of modern physics* **82**, 3045 (2010).
- [8] X.-L. Qi and S.-C. Zhang, Topological insulators and superconductors, *Reviews of Modern Physics* **83**, 1057 (2011).
- [9] W. A. Benalcazar, B. A. Bernevig, and T. L. Hughes, Quantized electric multipole insulators, *Science* **357**, 61 (2017).
- [10] W. A. Benalcazar, B. A. Bernevig, and T. L. Hughes, Electric multipole moments, topological multipole moment pumping, and chiral hinge states in crystalline insulators, *Physical Review B* **96**, 245115 (2017).
- [11] Z. Song, Z. Fang, and C. Fang, $(d-2)$ -dimensional edge states of rotation symmetry protected topological states, *Physical review letters* **119**, 246402 (2017).
- [12] J. Langbehn, Y. Peng, L. Trifunovic, F. von Oppen, and P. W. Brouwer, Reflection-symmetric second-order topological insulators and superconductors, *Physical review letters* **119**, 246401 (2017).
- [13] M. Geier, L. Trifunovic, M. Hoskam, and P. W. Brouwer, Second-order topological insulators and superconductors with an order-two crystalline symmetry, *Physical Review B* **97**, 205135 (2018).
- [14] F. Schindler, A. M. Cook, M. G. Vergniory, Z. Wang, S. S. Parkin, B. A. Bernevig, and T. Neupert, Higher-order topological insulators, *Science advances* **4**, eaat0346 (2018).
- [15] B. Xie, H.-X. Wang, X. Zhang, P. Zhan, J.-H. Jiang, M. Lu, and Y. Chen, Higher-order band topology, *Nature Reviews Physics* **3**, 520 (2021).
- [16] W. Zhang, X. Xie, H. Hao, J. Dang, S. Xiao, S. Shi, H. Ni, Z. Niu, C. Wang, K. Jin, *et al.*, Low-threshold topological nanolasers based on the second-order corner state, *Light: Science & Applications* **9**, 109 (2020).
- [17] H.-R. Kim, M.-S. Hwang, D. Smirnova, K.-Y. Jeong, Y. Kivshar, and H.-G. Park, Multipolar lasing modes from topological corner states, *Nature communications* **11**, 5758 (2020).
- [18] X. Lu, Y. Chen, and H. Chen, Orbital corner states on breathing kagome lattices, *Physical Review B* **101**, 195143 (2020).
- [19] Y. Zhang, D. Bongiovanni, Z. Wang, X. Wang, S. Xia, Z. Hu, D. Song, D. Jukić, J. Xu, R. Morandotti, *et al.*, Realization of photonic p -orbital higher-order topological insulators, *eLight* **3**, 5 (2023).
- [20] Y. Okamoto, G. J. Nilsen, J. P. Attfield, and Z. Hiroi, Breathing pyrochlore lattice realized in A-site ordered spinel oxides LiGaCr₄O₈ and LiInCr₄O₈, *Physical review letters* **110**, 097203 (2013).
- [21] M. Ezawa, Higher-order topological insulators and semimetals on the breathing kagome and pyrochlore lattices, *Physical*

- review letters **120**, 026801 (2018).
- [22] M. Weiner, X. Ni, M. Li, A. Alù, and A. B. Khanikaev, Demonstration of a third-order hierarchy of topological states in a three-dimensional acoustic metamaterial, *Science Advances* **6**, eaay4166 (2020).
- [23] F.-Y. Li, Y.-D. Li, Y. B. Kim, L. Balents, Y. Yu, and G. Chen, Weyl magnons in breathing pyrochlore antiferromagnets, *Nature communications* **7**, 12691 (2016).
- [24] Y. Tanaka, M. Yoshida, M. Takigawa, Y. Okamoto, and Z. Hiroi, Novel Phase Transitions in the Breathing Pyrochlore Lattice: ^7Li -NMR on $\text{LiInCr}_4\text{O}_8$ and $\text{LiGaCr}_4\text{O}_8$, *Physical Review Letters* **113**, 227204 (2014).
- [25] J. Rau, L. Wu, A. May, L. Poudel, B. Winn, V. Garlea, A. Huq, P. Whitfield, A. Taylor, M. Lumsden, *et al.*, Anisotropic exchange within decoupled tetrahedra in the quantum breathing pyrochlore $\text{Ba}_3\text{Yb}_2\text{Zn}_5\text{O}_{11}$, *Physical Review Letters* **116**, 257204 (2016).
- [26] G. Pokharel, H. S. Arachchige, T. J. Williams, A. F. May, R. S. Fishman, G. Sala, S. Calder, G. Ehlers, D. S. Parker, T. Hong, *et al.*, Cluster frustration in the breathing pyrochlore magnet $\text{LiGaCr}_4\text{S}_8$, *Physical Review Letters* **125**, 167201 (2020).
- [27] H. Yan, O. Benton, L. D. Jaubert, N. Shannon, *et al.*, Rank-2 U(1) spin liquid on the breathing pyrochlore lattice, *Physical Review Letters* **124**, 127203 (2020).
- [28] Z. He, Y. Gu, H. Wo, Y. Feng, D. Hu, Y. Hao, Y. Gu, H. C. Walker, D. T. Adroja, and J. Zhao, Neutron Scattering Studies of the Breathing Pyrochlore Antiferromagnet $\text{LiGaCr}_4\text{O}_8$, *Physical Review Letters* **127**, 147205 (2021).
- [29] Y. Tokura and N. Nagaosa, Orbital physics in transition-metal oxides, *science* **288**, 462 (2000).
- [30] X. Li and W. V. Liu, Physics of higher orbital bands in optical lattices: a review, *Reports on Progress in Physics* **79**, 116401 (2016).
- [31] S. Xu and C. Wu, Orbital-active Dirac materials from the symmetry principle, *Quantum Frontiers* **1**, 24 (2022).
- [32] G. Wirth, M. Ölschläger, and A. Hemmerich, Evidence for orbital superfluidity in the P-band of a bipartite optical square lattice, *Nature Physics* **7**, 147 (2011).
- [33] R. Sibille, N. Gauthier, E. Lhotel, V. Porée, V. Pomjakushin, R. A. Ewings, T. G. Perring, J. Ollivier, A. Wildes, C. Ritter, *et al.*, A quantum liquid of magnetic octupoles on the pyrochlore lattice, *Nature physics* **16**, 546 (2020).
- [34] N. Tang, Y. Gritsenko, K. Kimura, S. Bhattacharjee, A. Sakai, M. Fu, H. Takeda, H. Man, K. Sugawara, Y. Matsumoto, *et al.*, Spin-orbital liquid state and liquid-gas metamagnetic transition on a pyrochlore lattice, *Nature Physics* **19**, 92 (2023).
- [35] W. V. Liu and C. Wu, Atomic matter of nonzero-momentum Bose-Einstein condensation and orbital current order, *Physical Review A* **74**, 013607 (2006).
- [36] C. Wu and S. D. Sarma, $p_{x,y}$ -orbital counterpart of graphene: Cold atoms in the honeycomb optical lattice, *Physical Review B* **77**, 235107 (2008).
- [37] Y. Chen, Y. Yin, Z.-K. Lin, Z.-H. Zheng, Y. Liu, J. Li, J.-H. Jiang, and H. Chen, Observation of topological p-orbital disclination states in non-Euclidean acoustic metamaterials, *Physical Review Letters* **129**, 154301 (2022).
- [38] Y. Hatsugai and I. Maruyama, Z_Q topological invariants for Polyacetylene, Kagome and Pyrochlore lattices, *Europhysics Letters* **95**, 20003 (2011).
- [39] T. Kariyado, T. Morimoto, and Y. Hatsugai, Z_N Berry Phases in Symmetry Protected Topological Phases, *Physical review letters* **120**, 247202 (2018).
- [40] H. Araki, T. Mizoguchi, and Y. Hatsugai, Z_Q Berry phase for higher-order symmetry-protected topological phases, *Physical Review Research* **2**, 012009 (2020).
- [41] H. Wakao, T. Yoshida, H. Araki, T. Mizoguchi, and Y. Hatsugai, Higher-order topological phases in a spring-mass model on a breathing kagome lattice, *Physical Review B* **101**, 094107 (2020).
- [42] Z.-X. Li, Y. Cao, X. Wang, and P. Yan, Second-order topological solitonic insulator in a breathing square lattice of magnetic vortices, *Physical Review B* **101**, 184404 (2020).
- [43] Y. Otsuka, T. Yoshida, K. Kudo, S. Yunoki, and Y. Hatsugai, Higher-order topological Mott insulator on the pyrochlore lattice, *Scientific reports* **11**, 20270 (2021).
- [44] J. Wu, S. Ghosh, Y. Gan, Y. Shi, S. Mandal, H. Sun, B. Zhang, T. C. Liew, R. Su, and Q. Xiong, Higher-order topological polariton corner state lasing, *Science Advances* **9**, eadg4322 (2023).
- [45] Z. Yang, F. Gao, X. Shi, X. Lin, Z. Gao, Y. Chong, and B. Zhang, Topological acoustics, *Physical review letters* **114**, 114301 (2015).
- [46] G. Ma, M. Xiao, and C. T. Chan, Topological phases in acoustic and mechanical systems, *Nature Reviews Physics* **1**, 281 (2019).
- [47] H. Xue, Y. Yang, and B. Zhang, Topological acoustics, *Nature Reviews Materials* **7**, 974 (2022).
- [48] W. Zhu, W. Deng, Y. Liu, J. Lu, H.-X. Wang, Z.-K. Lin, X. Huang, J. Jiang, and Z. Liu, Topological phononic metamaterials, *Reports on Progress in Physics* (2023).
- [49] T. Fukui, Y. Hatsugai, and H. Suzuki, Chern numbers in discretized Brillouin zone: efficient method of computing (spin) Hall conductances, *Journal of the Physical Society of Japan* **74**, 1674 (2005).
- [50] R. Yu, X. L. Qi, A. Bernevig, Z. Fang, and X. Dai, Equivalent expression of Z_2 topological invariant for band insulators using the non-Abelian Berry connection, *Physical Review B* **84**, 075119 (2011).
- [51] M. Miličević, G. Montambaux, T. Ozawa, O. Jamadi, B. Real, I. Sagnes, A. Lemaître, L. Le Gratiet, A. Harouri, J. Bloch, *et al.*, Type-III and tilted Dirac cones emerging from flat bands in photonic orbital graphene, *Physical Review X* **9**, 031010 (2019).
- [52] Q.-L. Sun, Y.-G. Peng, F. Gao, B. Li, and X.-F. Zhu, Montage Operation of Plaquette States in Acoustic Orbital Lattices with Type-III Dirac Points, *Physical Review Applied* **20**, 024025 (2023).
- [53] B. Hu, Z. Zhang, H. Zhang, L. Zheng, W. Xiong, Z. Yue, X. Wang, J. Xu, Y. Cheng, X. Liu, *et al.*, Non-Hermitian topological whispering gallery, *Nature* **597**, 655 (2021).
- [54] H. Xue, Y. Yang, G. Liu, F. Gao, Y. Chong, and B. Zhang, Realization of an acoustic third-order topological insulator, *Physical review letters* **122**, 244301 (2019).
- [55] G.-Q. Luo, G.-H. Huang, and Z.-F. Xu, Bosonic Weyl excitations induced by p -orbital interactions in a cubic optical lattice, *arXiv preprint arXiv:2303.00210* (2023).
- [56] F. K. Kunst, G. van Miert, and E. J. Bergholtz, Lattice models with exactly solvable topological hinge and corner states, *Physical Review B* **97**, 241405 (2018).
- [57] M. Ezawa, Higher-order topological electric circuits and topological corner resonance on the breathing kagome and pyrochlore lattices, *Physical Review B* **98**, 201402 (2018).
- [58] D. Khomskii, Orbital physics: glorious past, bright future, *ECS Journal of Solid State Science and Technology* **11**, 054004 (2022).
- [59] X. Lu and E. Arrighoni, Dispersive spectrum and orbital order of spinless p-band fermions in an optical lattice, *Physical Review B* **79**, 245109 (2009).
- [60] J. Schulz, J. Noh, W. A. Benalcazar, G. Bahl, and G. von Freymann, Photonic quadrupole topological insulator using orbital-induced synthetic flux, *Nature communications* **13**,

- 6597 (2022).
- [61] M. Lewenstein and W. V. Liu, Orbital dance, *Nature Physics* **7**, 101 (2011).
- [62] P. Soltan-Panahi, D.-S. Lühmann, J. Struck, P. Windpassinger, and K. Sengstock, Quantum phase transition to unconventional multi-orbital superfluidity in optical lattices, *Nature Physics* **8**, 71 (2012).
- [63] M. Milićević, T. Ozawa, G. Montambaux, I. Carusotto, E. Galopin, A. Lemaître, L. Le Gratiet, I. Sagnes, J. Bloch, and A. Amo, Orbital edge states in a photonic honeycomb lattice, *Physical review letters* **118**, 107403 (2017).
- [64] M. Slot, S. Kempkes, E. Knol, W. Van Weerdenburg, J. Van Den Broeke, D. Wegner, D. Vanmaekelbergh, A. Khajetoorians, C. M. Smith, and I. Swart, p-band engineering in artificial electronic lattices, *Physical Review X* **9**, 011009 (2019).
- [65] Y. Iqbal, T. Müller, P. Ghosh, M. J. Gingras, H. O. Jeschke, S. Rachel, J. Reuther, and R. Thomale, Quantum and classical phases of the pyrochlore Heisenberg model with competing interactions, *Physical Review X* **9**, 011005 (2019).
- [66] Y.-B. Yang, J.-H. Wang, K. Li, and Y. Xu, Higher-order topological phases in crystalline and non-crystalline systems: a review, *arXiv preprint arXiv:2309.03688* (2023).
- [67] M. Kim, Z. Jacob, and J. Rho, Recent advances in 2D, 3D and higher-order topological photonics, *Light: Science & Applications* **9**, 130 (2020).
- [68] H. Chen, Simulating the Palmer-Chalker state in an orbital superfluid, *Physical Review A* **101**, 063601 (2020).
- [69] H. Chen, C. Wu, and X. Xie, Emergent Weyl fermions in an orbital multipolar ordered phase, *Physical Review B* **105**, 205132 (2022).
- [70] A. Kłosiński, W. Brzezicki, A. Lau, C. E. Agrapidis, A. M. Oleś, J. van Wezel, and K. Wohlfeld, Topology of chalcogen chains, *Physical Review B* **107**, 125123 (2023).
- [71] Z. Cheng, Y.-j. Guan, H. Xue, Y. Ge, D. Jia, Y. Long, S.-q. Yuan, H.-x. Sun, Y. Chong, and B. Zhang, Three-dimensional flat Landau levels in an inhomogeneous acoustic crystal, *arXiv preprint arXiv:2308.14313* (2023).
- [72] E. Zhao and W. V. Liu, Orbital Order in Mott Insulators of Spinless p -Band Fermions, *Phys. Rev. Lett.* **100**, 160403 (2008).
- [73] F. Gao, X. Xiang, Y.-G. Peng, X. Ni, Q.-L. Sun, S. Yves, X.-F. Zhu, and A. Alù, Orbital topological edge states and phase transitions in one-dimensional acoustic resonator chains, *Nature Communications* **14**, 8162 (2023).
- [74] Y.-C. Jiang, T. Kariyado, and X. Hu, Higher-Order Topology in Honeycomb Lattice with Y-Kekulé Distortions, *Journal of the Physical Society of Japan* **93**, 033703 (2024).